Enhancing Forward-Looking Image Resolution: Combining Low-Rank and Sparsity Priors

Junkui Tang, Zheng Liu, Lei Ran, Rong Xie, and Jikai Qin, *Graduate Student Member, IEEE*

***Abstract*— Compressed sensing (CS)-based imaging technology has attracted a lot of interest because it can enhance imaging resolution. Targets of interest for forward-looking imaging radar are typically few in comparison to the entire imaging region. This sparsity allows for the natural application of CS to the reconstruction of high-resolution forward-looking images. However, conventional CS-based imaging methods can only perform well when the signal-to-noise ratio (SNR) is high. Strong noise in radar imaging prevents the CS-based methods from producing excellent imaging results. Inspired by the low-rank property of the received radar target echo and the sparsity of the forward-looking image targets, we present a combined low-rank and sparse prior restricted model for forward-looking imaging with a multichannel array radar to overcome strong noise. To solve the low-rank joint sparse double prior constraint optimization problem, an augmented Lagrange multiplier (ALM) reconstruction method under the framework of the alternating direction multiplier method (ADMM) is proposed. Finally, the results of simulation and real measurement data indicate that our presented method is fairly effective at enhancing the azimuth resolution and robustness of forward-looking radar imaging in comparison to other current methods.**

***Index Terms*— Alternating direction multiplier method (ADMM), augmented Lagrange multiplier (ALM), compressed sensing (CS), forward-looking imaging, low-rank and sparse prior, strong noise.**

I. Introduction

IN SEVERAL civil and military applications, such as precise navigation, autonomous landing, and topographic mapping, forward-looking high-resolution imaging is critical importance [1], [2], [3], [4], [5]. Unfortunately, the mechanism behind Doppler beam sharpening (DBS) or standard monostatic synthetic aperture radar (SAR) prohibits their forward-looking high-resolution imaging, i.e., terrain sites symmetrically located along the flight route have identical Doppler histories, which makes the Doppler frequency gradient in the flight direction relatively tiny [6], [7]. Theoretically, we can expand the antenna aperture to improve the forward-looking image resolution. In practical application scenarios, the antenna aperture size is usually constrained by platforms like missiles and unmanned aerial vehicles (UAVs), which results in the ineffective method of increasing the aperture size to improve the forward-looking resolution [8], [9], [10]. Therefore, low azimuth resolution inhibits the quality of imaging in the forward-looking direction for practical applications [11], [12], [13].

In recent years, forward-looking scanning radar imaging based on the deconvolution approach has been described and demonstrated to be useful for boosting image azimuth resolution [14], [15], [16]. This is due to the fact that the forward-looking image azimuth echo signal is a convolution of the spatial distribution of the target and the antenna pattern [17]. However, because the antenna design is a low-pass filter, the strength of high-frequency noise is amplified during deconvolution, which has an effect on the azimuth resolution. Consequently, the traditional deconvolution method is an ill-posed problem [18]. Many strategies have been offered in prior research to alleviate the discomfort of deconvolution. Huang et al. [11] resolved the issue of noise amplification in deconvolution imaging using the truncated singular decomposition approach within the context of algebraic theory, thereby attaining effective augmentation of forward-looking imaging angular resolution. Tan et al. [19] proposed a maximum likelihood (ML) method for I/Q channel modeling of forward-looking scanning radar, which can accurately estimate targets by maximizing the likelihood function. Xia et al. [20] designed a multichannel deconvolution super-resolution signal model of forward-looking imaging that greatly alleviates the ill-posed problem of the traditional single-channel deconvolution through joint processing of multiple channels. Zhang et al. [21] proposed a total variation (TV) forward-looking high-resolution imaging approach using the truncated singular value decomposition (TSVD) strategy, which increases noise robustness by removing small singular values of the antenna convolution matrix. Furthermore, based on the Bayesian theory, Zha et al. [22] used a Laplacian distribution to describe the prior information of the target and the maximum a posteriori probability criterion to solve the relevant deconvolution issue, thereby attaining the azimuth super-resolution of scanning radar. As mentioned in the above literature, forward-looking super-resolution imaging has been made possible with the use of deconvolution methods. However, in most papers, the amplitude absolute value pattern is adopted without considering the influence of phase on the

Manuscript received 29 September 2022; revised 11 December 2022 and 3 January 2023; accepted 11 January 2023. Date of publication 16 January 2023; date of current version 26 January 2023. This work was supported in part by the National Natural Science Foundation of China under Grant 62001346, in part by the China Postdoctoral Science Foundation under Grant 2019M663632, and in part by the Seed Funding Project of Multisensor Intelligent Detection and Recognition Technologies Research and Development Center of CASC under Grant ZZJJ202102. *(Corresponding author: Zheng Liu.)*

The authors are with the National Laboratory of Radar Signal Processing, Xidian University, Xi'an 710071, China (e-mail: tjk_0622@126.com; lz@xidian.edu.cn).

Digital Object Identifier 10.1109/TGRS.2023.3237332

pattern. According to the antenna theory, this pattern is difficult to realize in reality [23], [24].

At present, compressed sensing (CS) technology has been introduced into radar high-resolution imaging applications, which can use low-dimensional observation data to achieve accurate recovery of high-dimensional sparse signals, provided that the targets in the imaging are sparse [25], [26], [27]. In actual radar imaging, the number of intense scattering centers is far less than the total number of image pixels [28], [29], [30], [31]. Therefore, it is feasible to realize forward-looking high-resolution imaging based on CS. Giusti et al. [32] analyzed in detail the performance of using CS to reconstruct super-resolution inverse SAR (ISAR) images and the comparison between CS and traditional super-resolution technologies. They demonstrated that CS is applicable to ISAR images. In [33], under sub-Nyquist rate sampling, a new CS-SAR imaging method using a multimeasurement vector (MMV) model has been used to achieve high-quality imaging, which can greatly save the computational cost in time and memory. Also, Ao et al. [34] realized the accurate reconstruction of bistatic ISAR (Bi-ISAR) images by joint CS optimized weighting and improved Fourier basis. However, considerable noise is typically unavoidable in radar imaging. The insufficient sparsity of noise distribution will have a significant impact on the reconstruction of target information, which poses a challenge to the existing high-resolution imaging techniques based on CS. The sparsity prior assumption is the most widely used method for overcoming severe noise. Nevertheless, a single sparsity constraint cannot solve every problem. Qiu et al. [35] presented a joint low-rank and sparse prior (JLRS) ISAR imaging method. The low-rank property of the echo signal and the sparsity of the target are used to improve ISAR imaging performance when data are lost randomly. However, because the noise is not constrained in the imaging model, the performance of the imaging results will deteriorate in the strong noise environment. Zhang et al. [36] found that combining a nonlocal total variation (NLTV) constraint with local sparsity can overcome strong noise and eliminate some spurious strong scattering targets or clutter in ISAR imaging while simultaneously preserving the form and geometry of target regions. Furthermore, Zeng et al. [37], inspired by the sparsity and low-rank of the 2-D distribution of the target, presented a novel ISAR reconstruction method. The experimental results demonstrate that this approach provides superior image quality and noise resistance. However, the reconstruction performance is not optimal due to the use of the zero norm of the 2-D matrix as the sparsity constraint. Zhang et al. [38] proposed a weighted CS (WCS) method for ISAR image generation, which improved the robustness of the traditional CS algorithm through different weight constraints on the target and noise.

In the above literature, we observe that adding additional prior knowledge can increase the performance of the CS-based imaging. In light of this, we propose a multichannel array radar forward-looking imaging model based on combining sparse and low-rank priors. Our model takes into account the fact that the target is sparse in the forward-looking region and that the received signal of a multichannel array radar system exhibits substantial intracorrelations. Specifically, the signal matrix is recovered by a low-rank constraint, and the sparsity of target distribution is used to detect and differentiate the strong scattering centers and noise spots to eliminate false or unreliable strong scattering points. Moreover, with regard to the resulting double optimization issue, the alternating direction multiplier method (ADMM) [39] can effectively solve the constrained optimization problem and converge mild. The ADMM has been effectively used in multiple joint optimizations of ISAR or SAR imaging [40], [41], [42]. Therefore, under the ADMM framework, this article proposes an augmented Lagrange multiplier (ALM) method for efficiently solving our proposed optimization problem model.

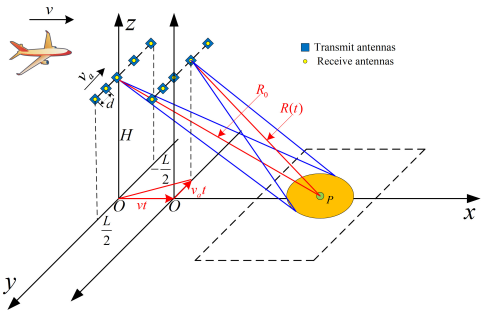

Fig. 1. Forward-looking imaging model of the multichannel array radar.

The structure of this article is as follows. Section II presents the forward-looking imaging model of multichannel array radar and the CS-based forward-looking super-resolution imaging method. In Section III, a forward-looking imaging method that combines low-rank and sparsity is proposed in detail. In Section IV, the experimental results are presented to demonstrate the effectiveness of our proposed method, and in Section V, a conclusion is given.

II. Signal Model

The forward-looking imaging system model of the multichannel array radar is depicted in Fig. 1. The N multiple integrated transceiver antennas are positioned on a radar platform with a height of H and a length of L. The radar platform moves at speed v, and N antennas are linearly aligned at equal intervals d, sequentially sending signals and receiving echoes. Assume there is a point target $P(x_0, y_0, 0)$ on the ground directly in front of the radar platform, and the azimuth coordinate of the nth antenna is y_n. If t denotes the slow time, v_a is the equivalent moving speed of the antenna, i.e., $y_n = v_a t$, then the oblique distance from the point target P to the nth antenna is

$$R(t) = \sqrt{(vt - x_0)^2 + (-v_a t - y_0)^2 + H^2}. \tag{1}$$

The expansion of (1) by the second order of Taylor is

$$R(t) = R_0 - \left(\frac{x_0}{R_0}v - \frac{y_0}{R_0}v_a\right)t + \frac{H^2\left(v_a^2 + v^2\right) + \left(v y_0 + v_a x_0\right)^2}{2{R_0}^3}t^2 + o\left(t^2\right) \tag{2}$$

where $R_0 = (x_0{}^2 + y_0{}^2 + H^2)^{1/2}$ is the slant distance from the scattering point P to the center of the array antenna.

The distance R_0 is usually quite large in forward-looking radar imaging, and small platforms such as UAVs move slowly, so the second-order term of the Taylor expansion in (2) is very small and can be ignored, then (2) can be approximated as

$$R(t) \approx R_0 - \left(\frac{x_0}{R_0}v - \frac{y_0}{R_0}v_a\right)t. \tag{3}$$

Suppose that the radar transmits linear frequency modulation (LFM) signal as

$$s(\tau) = w_r(\tau)\exp\left[j2\pi\left(f_c\tau + \frac{\gamma}{2}\tau^2\right)\right] \tag{4}$$

where f_c is the carrier frequency, τ denotes the fast time, γ is the chirp rate, and w_r stands for the range window function. After the echo is compressed by matched filtering, it can be expressed as

$$S_{\mathrm{rc}}(\tau, t) = C \cdot \sin c\left[\pi B\left(\tau - \frac{2R(t)}{c}\right)\right] \cdot \exp\left(-j4\pi\frac{R(t)}{\lambda}\right) \tag{5}$$

where C represents the scattering point's complex scattering coefficient, c is the light velocity, λ is the wavelength, and B stands for the signal bandwidth. Then, the range walk correction factor is constructed for the echo signal after pulse compression in the frequency domain to eliminate the impact of platform motion on the echo signal. The echo signal after range walk correction can be expressed as

$$\begin{aligned} S_{\mathrm{rc}}(\tau, t) &= C \cdot \sin c\left[\pi B\left(\tau - \frac{2R_0}{c}\right)\right] \cdot \exp\left(-j4\pi\frac{R(t)}{\lambda}\right) \\ &\approx C \cdot \sin c\left[\pi B\left(\tau - \frac{2R_0}{c}\right)\right] \cdot \exp\left(-j\pi\frac{4R_0}{\lambda}\right) \\ &\quad \cdot \exp\left(j2\pi\frac{2v_a y_0}{\lambda R_0}t\right) \cdot \exp\left(j2\pi\frac{2vx_0}{\lambda R_0}t\right) \end{aligned} \tag{6}$$

where $(2v_a y_0/\lambda R_0)$ and $(2vx_0/\lambda R_0)$ are the Doppler frequency caused by the equivalent motion of the array antenna and the motion of the platform, respectively. In a range bin (i.e., x_0 is a fixed value), the slope of the Doppler frequency caused by the platform motion along the azimuth direction is $d(2vx_0/\lambda R_0)/dy_0 = (2vx_0 y_0/\lambda R_0^3)$. It is generally defined that the front $\pm 10^\circ$ of the moving platform is the forward-looking imaging area. Therefore, there is $y_0 \ll x_0$, and the Doppler frequency $(2vx_0/\lambda R_0)$ changes little in the azimuth direction. This is why it is impossible to achieve forward-looking high-resolution radar imaging by relying only on the traditional monostatic SAR imaging technology.

Assuming that the echo contains M range bins, ignore the fixed term $\exp(-j\pi(4R_0/\lambda))$ in (6) and cancel the phase factor $\exp(j2\pi(2vx_0/\lambda R_0)t)$, then the 2-D echo matrix S_{rc} after range compression can be expressed as

$$S_{\mathrm{rc}} = Y + E = AX + E \tag{7}$$

where $Y \in C^{N\times M}$ and $E \in C^{N\times M}$ are the signal matrix and noise matrix, respectively. $X \in C^{\overline{N}\times M}(\overline{N} > N)$ represent the 2-D super-resolution imaging. $A \in C^{N\times\overline{N}}$ denotes the dictionary matrix for the dimension of azimuth, and it can be expressed as

$$A = [a_1, \ldots, a_N], \quad a_n = \exp[-j2\pi \cdot f_d(n).t], \ 0 \le n \le \overline{N} \tag{8}$$

where $f_d = [1 : \overline{N}]\Delta f_d$, with $\overline{N} = f_r/\Delta f_d$.

Based on the a priori knowledge that targets are sparsely distributed in space, we can reconstruct the scattering intensity matrix X of the target through the following constrained optimization problem:

$$\min_X \|X\|_0, \quad \text{s.t. } \|S_{\mathrm{rc}} - AX\|_F^2 \le \varepsilon \tag{9}$$

where $\|\cdot\|_0$ denotes the l_0-norm of matrix, $\|\cdot\|_F$ denotes a matrix's Frobenius norm, and ε is a small constant that is determined by the level of noise. Formally, (8) is an MMV solution problem, which can be solved by the Bayesian algorithms [43], [44] and iterative reweighting algorithms [45], [46]. However, in practical applications, there is usually a strong noise in the echo. No sparsity of noise distribution will seriously affect the reconstruction of target information, resulting in the loss of important scattering points and the appearance of false points in the forward-looking imaging results.

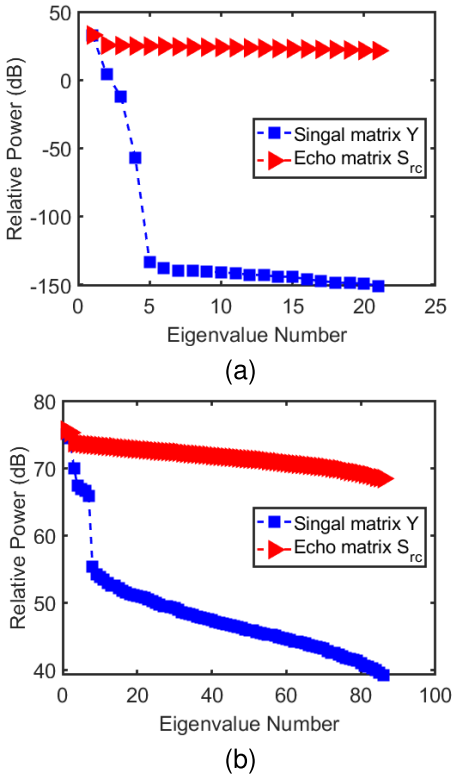

Fig. 2. Distribution of singular value of signal matrix Y and echo matrix S_{rc} (SNR = 5 dB). (a) Simulation data. (b) Real data.

III. Proposed Method

A. Low-Rank Property Analysis

Imaging of the CS-based systems is essentially an ill-posed problem for which there is no unique solution, particularly in the presence of significant noise [47]. Introducing appropriate

prior knowledge helps decrease the solving equation's ill-posedness [31], [48], [49]. In this section, we study the low-rank characteristic of the signal matrix received by forward-looking imaging. First, according to the rank inequalities of matric, the rank of signal matrix Y satisfies the following conditions:

$$\operatorname{rank}(Y) = \operatorname{rank}(AX) \le \operatorname{rank}(X). \tag{10}$$

Formula (10) shows that if the image matrix X satisfies the low-rank property, then Y must also satisfy the low-rank property. In fact, there is a lot of redundant information in the generated high-quality image, and the area we focus on only accounts for a small part, which indicates that there are multiple complete zero columns or rows in the image, that is, the image matrix X is low-rank. Consequently, the received signal matrix Y has the characteristic of low-rank. However, in a strong noise environment, the echo matrix S_{rc} is not low-rank. Fig. 2(a) and (b) depicts the normalized singular values of the signal matrix Y and echo matrix S_{rc} used in Section IV-A simulated point target experiment and Section IV-C real data surface target experiment, respectively.

As can be seen from Fig. 2(a), the singular value distribution of the actual echo matrix S_{rc} decays gradually. In contrast, the distribution of signal matrix Y singular values decays rapidly, indicating that the signal matrix Y has a low-rank characteristic. Furthermore, the singular values have the same change trend in real data, as shown in Fig. 2(b). Therefore, to increase the accuracy of reconstruction in forward-looking imaging processing, it is possible to take advantage of both the sparse and low-rank properties.

B. Proposed Combine Low-Rank and Sparse Forward-Looking Imaging Model

In this section, the low-rank characteristics of the signal matrix and the sparse qualities of the targets are exploited in forward-looking image reconstruction to improve the capacity to suppress noise. When low-rank and sparse characteristic constraints are applied, the forward-looking imaging model can be expressed as

$$\begin{aligned} &\min_{X,Y,E} \operatorname{rank}(Y) + \lambda_1 \|X\|_0 + \lambda_2 \|E\|_F^2 \\ &\text{s.t. } Y = AX \\ &\quad Y + E = S_{\text{rc}} \end{aligned} \tag{11}$$

where $\operatorname{rank}(\cdot)$ denotes the rank function, λ_1 and λ_2 are the regularization parameters. λ_1 is used to balance l_0-norm, and the rank of Y, and λ_2 is related to noise.

Considering that the l_0-norm and the rank function $\operatorname{rank}(\cdot)$ problems are usually NP-hard. Therefore, we relax the l_0-norm to the l_1-norm and the $\operatorname{rank}(\cdot)$ to the nuclear norm. Then, the optimization issue in (11) can be changed into the convex optimization issue shown below

$$\begin{aligned} &\min_{X,Y,E} \|Y\|_* + \lambda_1 \|X\|_1 + \lambda_2 \|E\|_F^2 \\ &\text{s.t. } Y = AX \\ &\quad Y + E = S_{\text{rc}} \end{aligned} \tag{12}$$

where $\|Y\|_* := \sum_i \sigma_i$ represents the nuclear norm of Y, and σ_i is the ith singular value of Y.

C. Solution of the Proposed Model

Using the augmented Lagrange function, the optimization issue posed in (12) can be efficiently resolved within the ADMM framework. To facilitate calculation, we let $J = X$, and then the ADMM form of (12) is

$$\begin{aligned} &\min_{Y,J,E} \|Y\|_* + \lambda_1 \|J\|_1 + \lambda_2 \|E\|_F^2 \\ &\text{s.t. } Y - AX = 0, \\ &\quad S_{\text{rc}} - AX - E = 0, \\ &\quad X - J = 0. \end{aligned} \tag{13}$$

The representation for the augmented Lagrange function of (13) is

$$\begin{aligned} &L(Y, J, X, E, Q_1, Q_2, Q_3, u_1, u_2, u_3) \\ &\quad = \|Y\|_* + \lambda_1 \|J\|_1 + \lambda_2 \|E\|_F^2 \\ &\qquad + Q_1^T (Y - AX) + \frac{u_1}{2} \|Y - AX\|_F^2 \\ &\qquad + Q_2^T (S_{\text{rc}} - AX - E) + \frac{u_2}{2} \|S_{\text{rc}} - AX - E\|_F^2 \\ &\qquad + Q_3^T (X - J) + \frac{u_3}{2} \|X - J\|_F^2 \end{aligned} \tag{14}$$

where Q_1, Q_2, and Q_3 denote the Lagrange multiplier matrices, u_1, u_2, and u_3 represent the penalty coefficient, until a particular convergence condition is reached, and the ADMM approach is used to predict the optimal variables Y, J, X, E, Q_1, Q_2, and Q_3 alternately, that is, by estimating one while holding the others constant. The solution to (14) is as follows:

$$\begin{cases} Y^{k+1} = \arg\min\limits_{Y} \left\{ L\left(Y^k, J^k, X^k, E^k, Q_1^k, Q_2^k, Q_3^k\right) \right\} \\ J^{k+1} = \arg\min\limits_{J} \left\{ L\left(Y^{k+1}, J^k, X^k, E^k, Q_1^k, Q_2^k, Q_3^k\right) \right\} \\ X^{k+1} = \arg\min\limits_{X} \left\{ L\left(Y^{k+1}, J^{k+1}, X^k, E^k, Q_1^k, Q_2^k, Q_3^k\right) \right\} \\ E^{k+1} = \arg\min\limits_{E} \left\{ L\left(Y^{k+1}, J^{k+1}, X^{k+1}, E^k, Q_1^k, Q_2^k, Q_3^k\right) \right\} \\ Q_1^{k+1} = Q_1^k + \mu_1^k \left(S_{\text{rc}} - AX^{k+1} - E^{k+1}\right) \\ Q_2^{k+1} = Q_2^k + \mu_2^k \left(Y - AX^{k+1}\right) \\ Q_3^{k+1} = Q_3^k + \mu_3^k \left(X - J^{k+1}\right) \\ \mu_1^{k+1} = \rho_1 \mu_1^k \\ \mu_2^{k+1} = \rho_2 \mu_2^k \\ \mu_3^{k+1} = \rho_3 \mu_3^k \end{cases} \tag{15}$$

where ρ_1, ρ_2, and ρ_3 are ratios used to increase u_1, u_2, and u_3, respectively, and $\rho_1, \rho_2, \rho_3 > 1$.

1) Updating Y: First, the optimization problem of updating Y while fixing J, X, E, Q_1, Q_2, and Q_3 can be expressed as follows:

$$\begin{aligned} Y^{k+1} &= \arg\min_{Y} \left\| Y^k \right\|_* + \left(Q_1^k\right)^T \left(Y^k - AX^k\right) \\ &\quad + \frac{u_1}{2} \left\| Y^k - AX^k \right\|_F^2 \\ &= \arg\min_{Y} \frac{1}{Q_1^k} \left\| Y^k \right\|_* + \frac{1}{2} \left\| Y^k - R^k \right\|_F^2 \end{aligned} \tag{16}$$

where

$$R^k = AX^k + \frac{Q_1^k}{\mu_1^k}. \tag{17}$$

Using the singular value thresholding (SVT) algorithm [49], the minimization nuclear norm problem of (16) was resolved as follows:

$$Y^{k+1} = U^k \text{soft}\left(\Sigma^k, \frac{1}{Q_1^k}\right)\left(V^k\right)^H \tag{18}$$

where U^k, V^k, and Σ^k are the SVD results of R^k, i.e., $R^k = U^k\Sigma^k(V^k)^H$. U^k and V^k are the unitary matrices, which satisfy $U^k(U^k)^H = I$ and $V^k(V^k)^H = I$, respectively, and Σ^k is all zero besides the elements on the main diagonal. soft$(\cdot)$ represents a soft threshold function which is defined as

$$\text{soft}(\Theta, \alpha) = \max\left\{1 - \frac{\alpha}{\Theta(i,j)}, 0\right\} \tag{19}$$

where $\Theta(i, j)$ is a matrix, and α is a constant.

2) Updating J: Second, similar to updating Y, the optimization problem of updating J while fixing Y, X, E, Q_1, Q_2, and Q_3 can be expressed as

$$\begin{aligned} J^{k+1} &= \arg\min_J \lambda_1\left\|J^k\right\|_1 + \left(Q_3^k\right)^T\left(X^k - J^k\right) \\ &\quad + \frac{u_3}{2}\left\|X^k - J^k\right\|_F^2 \\ &= \arg\min_J \frac{\lambda_1}{Q_3^k}\left\|J^k\right\|_1 + \frac{1}{2}\left\|J^k - \left(X^k + \frac{Q_3^k}{\mu_3^k}\right)\right\|_F^2. \end{aligned} \tag{20}$$

Let $R_1^k = X^k + (Q_3^k/u_3^k) - (\lambda_1/Q_3^k)$, and $R_2^k = X^k + (Q_3^k/\mu_3^k) + (\lambda_1/Q_3^k)$. This l_1-norm minimization problem of (20) can be solved as

$$J^{k+1} = \max\left(0, R_1^k\right) + \min\left(0, R_2^k\right). \tag{21}$$

3) Updating X: Third, the following optimization problem of updating X, i.e.,

$$\begin{aligned} X^{k+1} &= \arg\min_X \left(Y^{k+1} - AX^k\right) \\ &\quad + \frac{1}{2}\left\|AX^k - \left(Y^{k+1} + \frac{Q_1^k}{\mu_1^k}\right)\right\|_F^2 \\ &\quad + \left(S_{\text{rc}} - AX^k - E^k\right) \\ &\quad + \frac{1}{2}\left\|AX^k - \left(S_{\text{rc}} - E^k + \frac{Q_2^k}{\mu_2^k}\right)\right\|_F^2 \\ &\quad + \left(X^k - J^{k+1}\right) + \frac{1}{2}\left\|X^k - \left(J^{k+1} + \frac{Q_3^k}{\mu_3^k}\right)\right\|_F^2. \end{aligned} \tag{22}$$

The minimization optimization issue of (22) can be resolved by the following:

$$\begin{aligned} X^{k+1} &= \left(A^TA + 2I\right)/I \\ &\quad \times\left\{A^T\left[S_{\text{rc}} - E^k + Y^{k+1} - \left(\frac{Q_1^k}{\mu_1^k} + \frac{Q_2^k}{\mu_2^k}\right)\right]\right. \\ &\quad \left. - \frac{Q_3^k}{\mu_3^k} + J^{k+1}\right\} \end{aligned} \tag{23}$$

where I represents a unit array, and $I \in C^{\overline{N}\times\overline{N}}$.

TABLE I

ALGORITHM: ALM–ADMM FOR SOLVING (13)

Input: Measurd data matrix $S_{rc} \in C^{N\times M}$, azimuth dictionary matrix $A \in C^{N\times\overline{N}}$, regularization parameter $\lambda_1, \lambda_2 > 0$; iteration number $k = 1$, $Q_1^1 = Q_2^1 = Q_3^1 = E^1 = Y^1 \in 0^{N\times M}$, $J^1 = X^1 \in 0^{\overline{N}\times M}$, $u_1^1, u_2^1, u_3^1 > 0$, and $\rho_1, \rho_2, \rho_3 > 1$.

While the stop condition is not reached, do

Update Y:

1. $R^k = AX^k + \frac{Q_1^k}{\mu_1^k}$, $R^k = U^k\Sigma^k\left(V^k\right)^H$
2. $Y^{k+1} = U^k soft\left(\Sigma^k, \frac{1}{Q_1^k}\right)\left(V^k\right)^H$

Update J:

3. $R_1^k = X^k + \frac{Q_3^k}{u_3^k} - \frac{\lambda_1}{Q_3^k}$, $R_2^k = X^k + \frac{Q_3^k}{\mu_3^k} + \frac{\lambda_1}{Q_3^k}$
4. $J^{k+1} = \max\left(0, R_1^k\right) + \min\left(0, R_2^k\right)$

Update X:

5. $X^{k+1} = \left(A^TA + 2I\right)/I\times$
$\left\{A^T\left[S_{rc} - E^k + Y^{k+1} - \left(\frac{Q_1^k}{\mu_1^k} + \frac{Q_2^k}{\mu_2^k}\right)\right] - \frac{Q_3^k}{\mu_3^k} + J^{k+1}\right\}$

Update E:

6. $E^{k+1} = \frac{\mu_2^k\left(S_{rc} - AX^{k+1} + \frac{Q_2^k}{\mu_2^k}\right)}{\lambda_2^k + \mu_2^k}$

Update $Q_1,\ Q_2,\ Q_3$:

7. $Q_1^{k+1} = Q_1^k + \mu_1^k\left(S_{rc} - AX^{k+1} - E^{k+1}\right)$
$Q_2^{k+1} = Q_2^k + \mu_2^k\left(Y - AX^{k+1}\right)$
$Q_3^{k+1} = Q_3^k + \mu_3^k\left(X - J^{k+1}\right)$

Update $\mu_1,\ \mu_2,\ \mu_3$:

8. $\mu_1^{k+1} = \rho_1\mu_1^k$
$\mu_2^{k+1} = \rho_2\mu_2^k$
$\mu_3^{k+1} = \rho_3\mu_3^k$
9. $k = k + 1$

end while

Output: X

4) Updating E: Finally, by fixing others, the update of E can be expressed as

$$\begin{aligned} E^{k+1} &= \arg\min_E \lambda_2\|E\|_F^2 + Q_2^T(S_{\text{rc}} - AX - E) \\ &\quad + \frac{u_2}{2}\|S_{\text{rc}} - AX - E\|_F^2 \\ &= \arg\min_E \frac{\lambda}{Q_2^k}\|E\|_F^2 + \frac{1}{2}\left\|S_{\text{rc}} - AX - E + \frac{Q_2^k}{\mu_2^k}\right\|_F^2. \end{aligned} \tag{24}$$

The solution to this optimization problem (24) can be obtained by

$$E^{k+1} = \frac{\mu_2^k\left(S_{\text{rc}} - AX^{k+1} + \frac{Q_2^k}{\mu_2^k}\right)}{\lambda_2^k + \mu_2^k}. \tag{25}$$

Finally, the whole ALM–ADMM algorithm solution process for the proposed forward-looking imaging model (13) is summarized in Table I.

TABLE II
SIMULATION RADAR PARAMETERS

Carrier Frequency	35 GHz
Bandwidth	150 MHz
Antenna length	0.4 m
Antenna number	94
Antenna number	94
Working distance	3000 m
Radar platform speed	150 m/s

TABLE III
AWR2243 CASCADE RADAR PARAMETERS

Carrier Frequency	78.7 GHz
Bandwidth	2.5 GHz
Antenna length	0.16 m
Antenna number	86
Max working distance	150 m

IV. EXPERIMENTAL RESULT AND ANALYSIS

In this section, validate the efficacy of our proposed model and methods using both the simulated and actual measured data. All the processed results are compared with the conventional methods, such as real-beam imaging, CS, WCS [38], and JLRS [35]. For convenience, our proposed forward-looking imaging method combining low-rank and sparsity is called FLI-CLRS. For all the experiments, some parameters are set as follows: $\rho_1 = \rho_2 = \rho_3 = 1.2$, $u_1^1 = u_2^1 = u_3^1 = 1.2/\|A\|_F^2$, and the maximum number of iterations is 200. The regularization parameters λ_1 and λ_2 are $[1, 3]$ and $[2, 3]$, respectively.

A. Simulated Point Target Results

The experiments on the simulated data are presented in this section to validate the proposed forward-looking imaging method. This simulation considers a Ka-band millimeter-wave radar and nine scattering point targets, as represented in Fig. 3(a). Table II gives the most important simulation parameters. According to the experimental parameters, we can calculate that the range resolution is 1 m, and the resolution in azimuth of real-beam imaging is 32 m. However, according to the experimental setup, in the azimuth direction, the distance between two adjacent targets is about 8 m, so the real-beam imaging method does not have the ability to distinguish three targets in the same range bin, as shown in Fig. 3(b). Fig. 3(c) shows the results of super-resolution imaging with the conventional CS method under free noise. It can be seen that the nine strong scattering point targets are clearly distinguishable, which indicates that the CS-based imaging method is suitable for forward-looking super-resolution imaging. Next, Gaussian white noise is added to the echo to generate a different signal-to-noise ratio (SNR) to verify the robustness of our FLI-CLRS method, where SNR is defined as

$$\mathrm{SNR} = 20\log_{10}\frac{\|S_{\mathrm{rc}}\|_F}{\|S_{\mathrm{rc}} - Y\|_F}. \tag{26}$$

First, we compare the performances of different methods, including CS, WCS, JLRS, and the proposed FLI-CLRS, under different SNRs. The images obtained by the four methods are given in Fig. 4. We can clearly see that the traditional CS imaging algorithm still fails to achieve a satisfactory high-resolution image even under SNR = 10 dB. Similarly, the WCS and JLRS methods can only reconstruct part of the target due to their limited noise suppression ability, and there is a defocus problem. On the contrary, the proposed FLI-CLRS can still obtain a clear and separable image of the target close to the image referenced in Fig. 3(c) even under a low SNR, which shows the superior performance of the proposed method.

Then, we use the image correlation coefficient (ICorrcoef) and root mean square error (RMSE) to further quantitatively compare the performance of different methods, in which ICorrcoef is defined as

$$\mathrm{ICorrcoef}(E_r, E_o) = \frac{|\langle \mathrm{vec}(E_r), \mathrm{vec}(E_o)\rangle|}{\|\mathrm{vec}(E_r)\|_2 \|\mathrm{vec}(E_o)\|_2} \tag{27}$$

where E_r and E_o represent the reference image and images generated by different methods, respectively. Furthermore, the RMSE is defined as

$$\mathrm{RMSE} = \frac{\left\|X - \hat{X}\right\|_F}{\|X\|_F} \tag{28}$$

where X is the raw data, and $\hat{X}$ is the recovered data. Smaller RMSE and higher ICorrcoef represent a method with better reconstruction performance and better image quality, respectively.

Set the radar echo SNR to -5, 0, 5, 10, and 15 dB, respectively, to model different noise conditions. Then, the RMSE and ICorrcoef results of 200 Monte Carlo experiments for different methods are shown in Fig. 5. Obviously, under the same SNR, the proposed FLI-CLRS method has a smaller RMSE and higher ICorrcoef than the other three methods, which demonstrates that the proposed method obtains better reconstruction accuracy. This further confirms the effectiveness of the presented method.

B. Real Data Point Target Results

Next, we use the measurement data to further compare the performance of our proposed method. As shown in Fig. 6(a), the experimental scene is one of the roads in Xidian University, Xi'an, China, and the target is two corner reflectors. We fixed the AWR2243 cascade radar on the tripod to collect experimental data as depicted in Fig. 6(b), in which the AWR2243 cascade radar operates in the MIMO radar mode and transmits frequency modulated continuous wave signals in time-sharing, including 12 transmitting antennas and 16 receiving antennas. In MIMO configuration, with 86 virtual array antennas in the azimuth axis and $\lambda/2$ antenna spacing. Meanwhile, Table III gives the key AWR2243 cascade radar operating parameters.

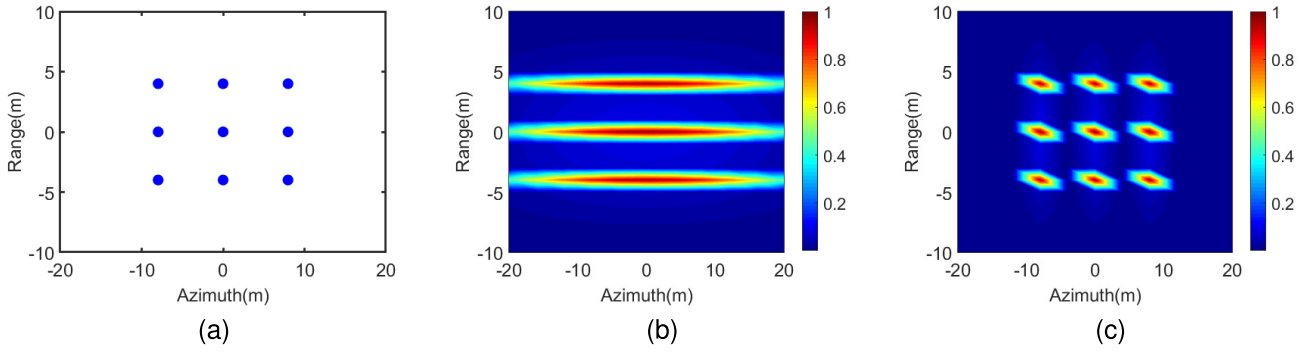

Fig. 3. (a) Nine point targets' distribution. (b) Real-beam imaging without noise. (c) CS-based imaging without noise.

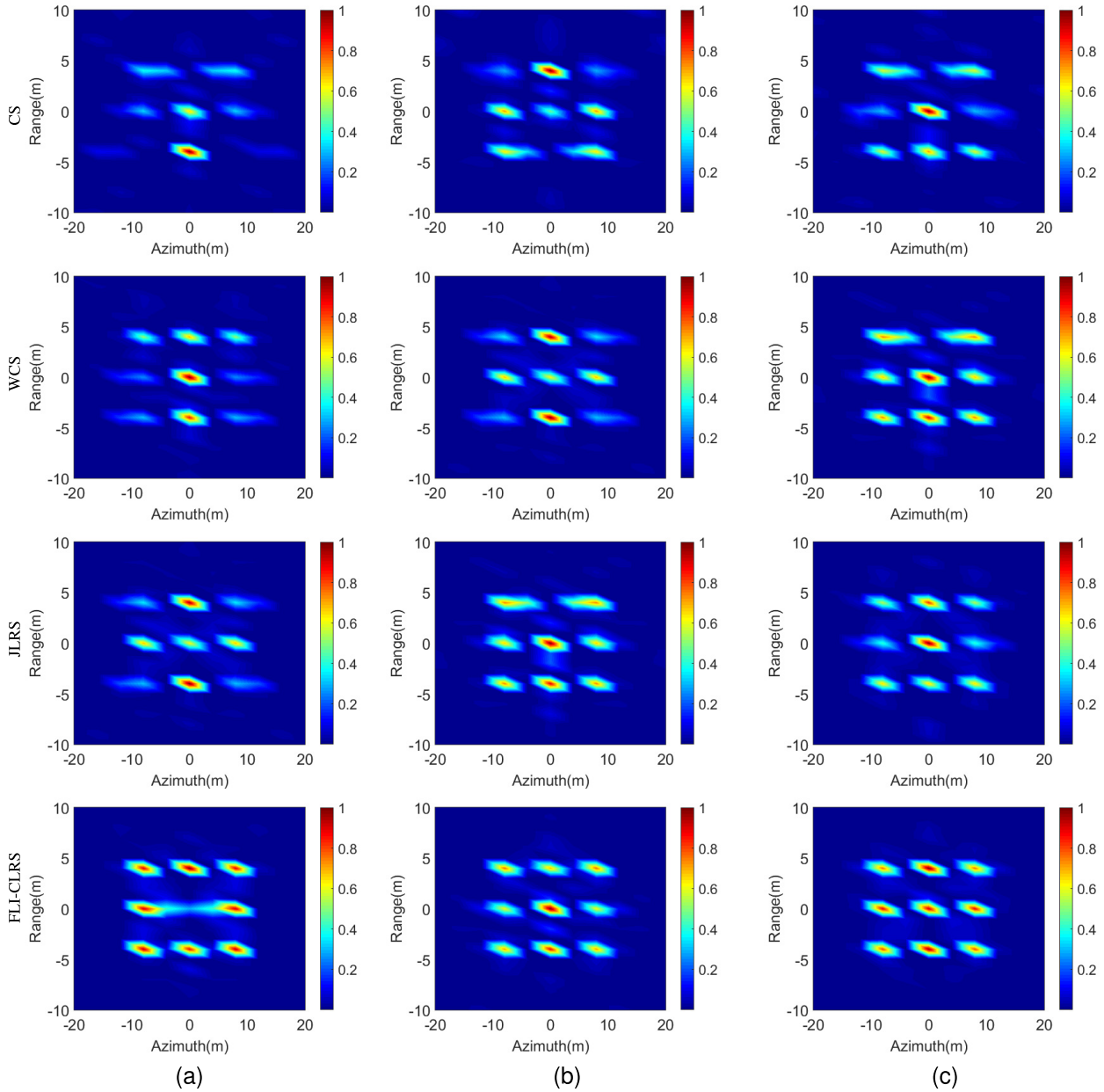

Fig. 4. Simulation imaging results of point targets with different imaging methods. (a) SNR = 0 dB. (b) SNR = 5 dB. (c) SNR = 10 dB.

It should be noted that in real data acquisition, we use the MIMO radar stationary platform, which is different from the signal model in Section II. First, the echo signal in Section II can ignore the impact of platform motion on imaging after platform range walk and phase correction processing, so it can be replaced by a stationary platform. Second, we extracted

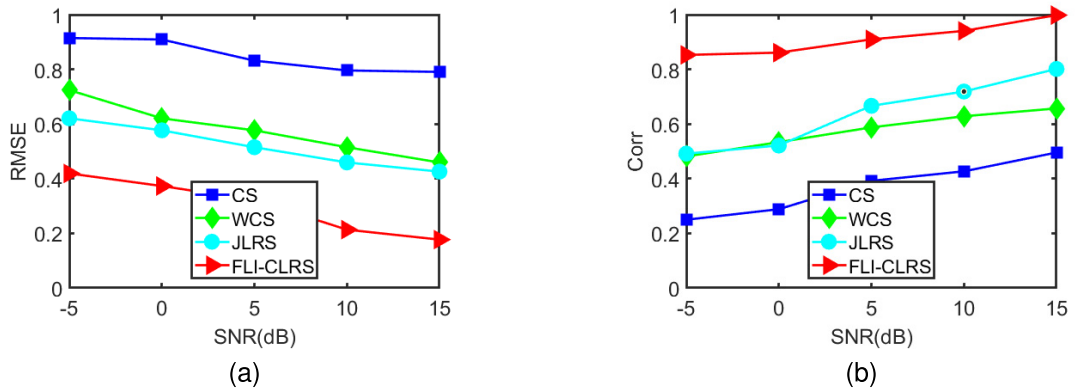

Fig. 5. Simulation imaging results of point targets' performance comparison with different imaging methods. (a) RMSE. (b) Corr.

Fig. 6. (a) Experimental scenario of point targets. (b) AWR2243 cascade radar.

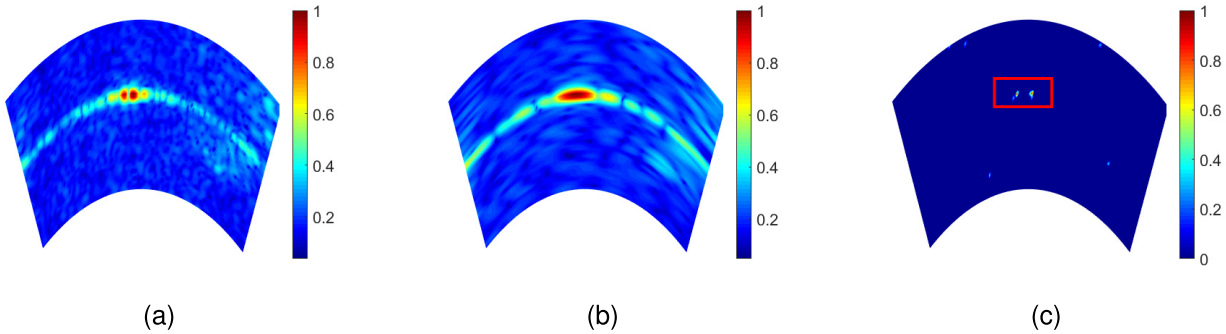

Fig. 7. Real data imaging results of point targets. (a) Real-beam imaging result of 86 antennas. (b) Real-beam imaging result of 24 antennas. (c) CS-based imaging result of 86 antennas.

the MIMO radar azimuth 86 antenna echo data for processing, that is, we still process range azimuth 2-D data in the subsequent, which will not affect the topic of forward-looking super-resolution imaging in this article. Therefore, it is reasonable for us to use MIMO radar to collect measured data in this article, which can also verify the target of this article: the azimuth super-resolution of a forward-looking image.

In this experiment, adjust the positions of the two targets so that they are placed in the same range unit and the distance between the azimuth center points is 0.20 m. Then, adjust the distance R_0 between the AWR2243 radar platform and the targets. When $R_0 = 9.5$ m, the real-beam imaging resolution can be calculated to be about 0.22 m. Therefore, as shown in Fig. 6(a), the full-aperture real-beam imaging method can distinguish between two targets. The real-beam imaging results obtained using the echoes of the 1–24 antennas are shown in Fig. 7(b). We can clearly see that the two targets cannot be distinguished at this time. Therefore, we can use the imaging results obtained from these 24 antenna echoes to validate the performance of our presented approach for super-resolution imaging. Meanwhile, we take the imaging result of the original

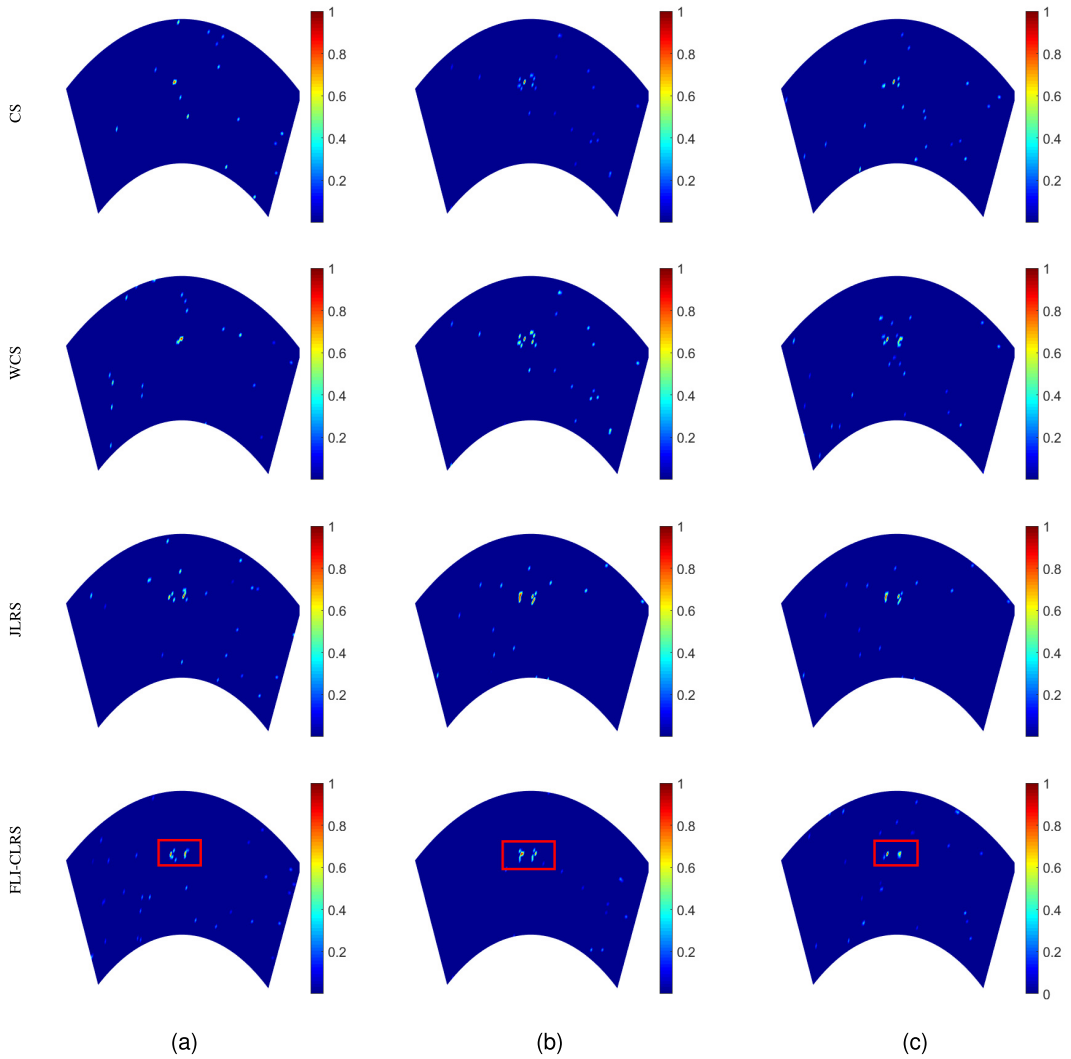

Fig. 8. Real data imaging results of point targets with different imaging methods. (a) SNR = 0 dB. (b) SNR = 5 dB. (c) SNR = 10 dB.

echo of the full aperture radar based on the CS method as the reference image, as shown in Fig. 7(c). We can clearly see that the two targets are clearly separable and have low sidelobes. Since the SNR in this scene is about 18 dB, we add Gaussian white noise to generate different SNRs.

Similar to the simulation point targets' experiment, Fig. 8 gives the imaging results of CS, WCS, JLRS, and FLI-CLRS with SNR = 0, 5, and 10 dB, respectively. From each column in Fig. 8, it can be seen that when SNR = 0 or 5 dB, strong noise destroys the sparsity of the target, resulting in the limited ability of the CS and WCS methods to constrain noise only depending on the l_1-norm, making it difficult to distinguish between the two targets or the appearance of false targets. Although both the JLRS method and the proposed FLI-CLRS method improve the imaging performance by using low-rank and sparse constraints, the JLRS method does not take noise into account in the optimization function, so the image obtained by the JLRS method is not as good as that produced by our proposed FLI-CLRS method, which indicates the superior performance of our proposed method. Of course, from each line in Fig. 8, we can see that the correlation between the target and the noise decreases with the increase in the SNR for the same method, and the imaging performance

Fig. 9. Experimental scenario of surface targets.

of all the methods improves. Then, as shown in Table IV, use RMSE and ICorrcoef to quantitatively evaluate the imaging results of different methods. We can clearly see that our

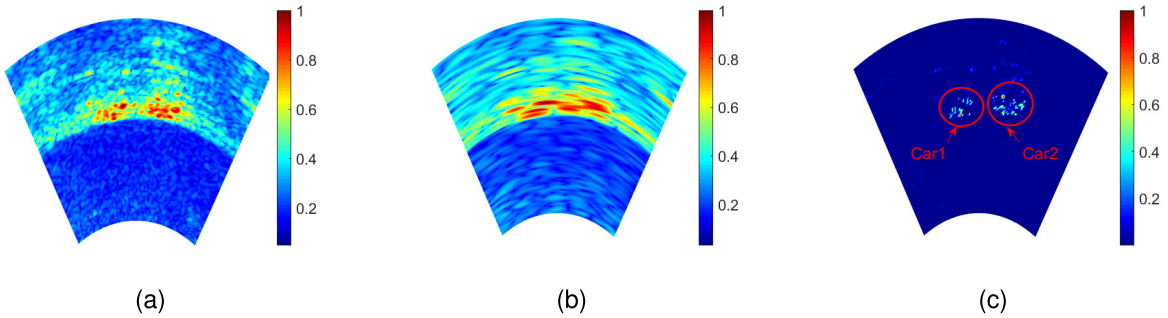

Fig. 10. Real data imaging results of surface target. (a) Real-beam imaging result of 86 antennas. (b) Real-beam imaging result of 24 antennas. (c) CS-based imaging result of 86 antennas.

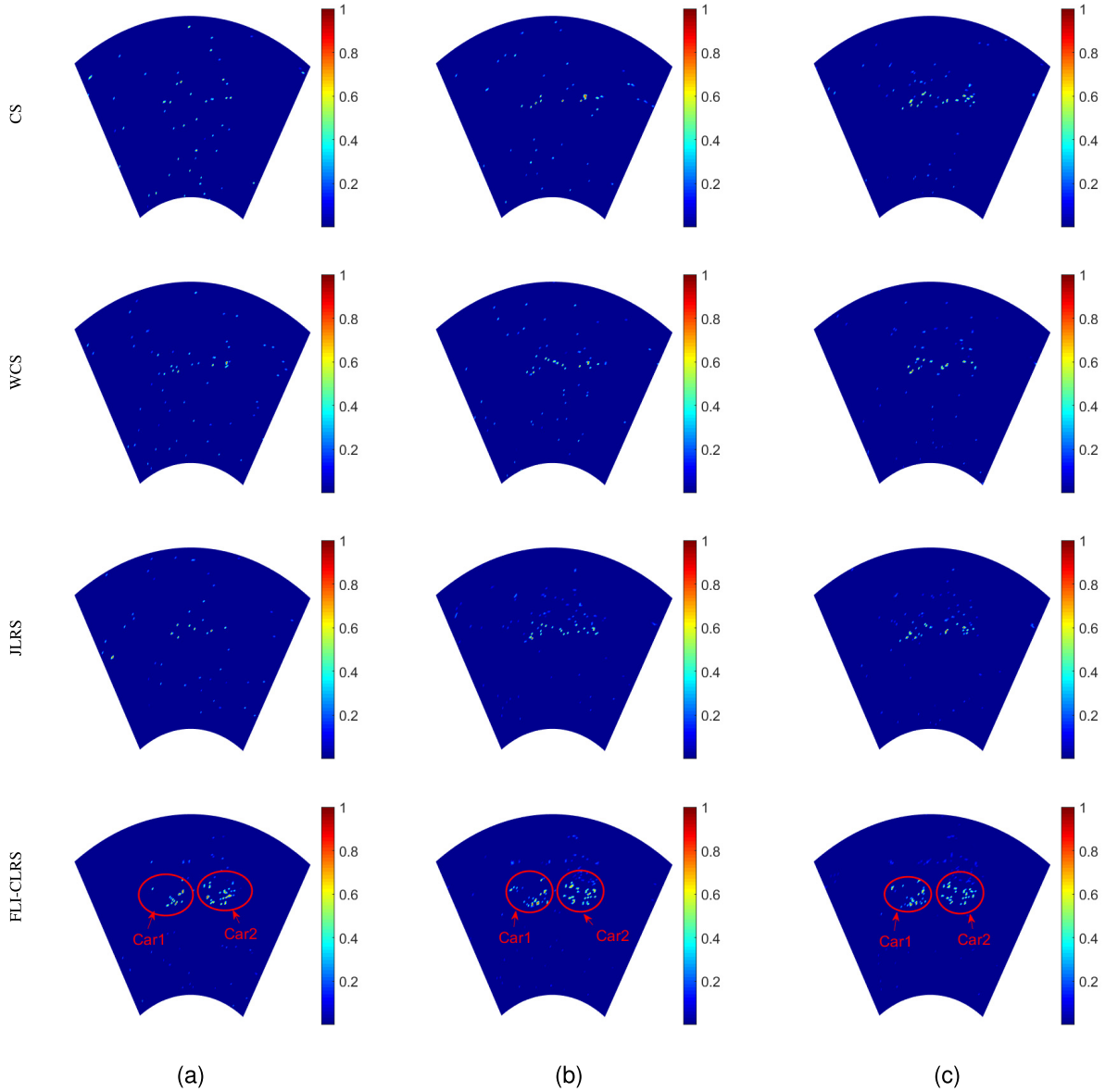

Fig. 11. Real data imaging results of surface targets with different imaging methods. (a) SNR = 0 dB. (b) SNR = 5 dB. (c) SNR = 10 dB.

proposed FLI-CLRS has superior super-resolution imaging performance.

C. Real Data Surface Target Results

Usually, in real forward-looking imaging scenarios, the objects we observe are surface targets, such as cars, ships, or bridges. Therefore, in this section, the availability of our proposed method is evaluated using a surface target. Similar to point target measurement, the experimental device is an AWR2243 cascade radar, and the parameter values are identical to those in Section IV-B. The experimental site is located in the parking lot of Xidian University, Xi'an, China,

TABLE IV
COMPARISON OF RMSE AND ICORRCOEF OF POINT TARGETS' IMAGING

Method	RMSE			ICorrcoef		
	0dB	5dB	10dB	0dB	5dB	10dB
CS	0.84	0.75	0.52	0.32	0.38	0.52
WCS	0.81	0.72	0.50	0.48	0.50	0.53
JLRS	0.70	0.45	0.32	0.72	0.75	0.77
FLR-CLRS	0.32	0.30	0.18	0.85	0.88	0.90

TABLE V
COMPARISON OF RMSE AND ICORRCOEF OF SURFACE TARGETS' IMAGING

Method	RMSE			ICorrcoef		
	0dB	5dB	10dB	0dB	5dB	10dB
CS	0.89	0.80	0.63	0.16	0.24	0.38
WCS	0.82	0.75	0.63	0.45	0.48	0.50
JLRS	0.50	0.44	0.35	0.46	0.50	0.65
FLR-CLRS	0.24	0.21	0.20	0.82	0.85	0.89

and the target is two cars, as shown in Fig. 9. Fig. 10(a) shows the image obtained by the real-beam imaging method based on full-aperture radar echo data, where two cars can be distinguished. When we only use the echo data of the 1–24 antennas and also use the real beam imaging method, the imaging result is depicted in Fig. 10(b). At this time, the two cars are overlapped and cannot be distinguished. Therefore, use these 24 antenna echoes to test the super-resolution imaging capability of our proposed method in terms of surface targets. Similarly, as shown in Fig. 10(c), we use the imaging results of the CS-based imaging method with the full aperture radar echo data as the reference image.

Fig. 11 shows the imaging results of different methods under three SNRs. We can clearly see that under the same SNR, both the conventional CS method and the WCS method generated images are difficult to distinguish between the two cars, and a large number of false targets appear. Although the JLRS method can roughly distinguish targets, there are still false targets. The proposed FLI-CLRS method can produce satisfactory imaging results, and the target is clear and distinguishable. Subsequently, ICorrcoef and RMSE of different methods were calculated, and the results are shown in Table V. We can clearly see from Table V that the FLI-CLRS method proposed by us has the highest Corr and the lowest RMSE, which proves the excellent performance of the method presented by us.

V. CONCLUSION

This article proposes a valid method to enhance the forward-looking radar image with limited aperture. In addition to the sparse nature of the target commonly used by the traditional CS-based imaging algorithms, the inherent relationship between the echo signals is used to improve the image quality. Specifically, a forward-looking high-resolution imaging method combining sparse and low-rank characteristics is presented, where low-rank refers to the energy of the echo signal that can be represented by several large eigenvalues when noise is not considered. Furthermore, an algorithm based on ALM–ADMM is presented to effectively solve the two constraints. Finally, based on the simulated and actual measured data, we demonstrate that the method can not only obtain forward-looking super-resolution imaging but also has noise robustness. When SNR is over 0 dB, the FLR-CLRS imaging method that we propose can produce at least four times the super-resolution imaging in simulation experiments and at least 3.5 times the super-resolution imaging in measured data experiments compared with the real beam imaging method.

It is important to note that the method presented in this article only suppresses the noise appearing in radar imaging, whereas the actual scene contains a great deal of clutter. If clutter is not suppressed, subsequent target detection will be affected. Therefore, future studies will consider suppressing both noise and clutter so that the proposed method can be applied to more scenarios.

REFERENCES

[1] Q. Zhang, J. Wu, Z. Li, Y. Miao, Y. Huang, and J. Yang, "PFA for bistatic forward-looking SAR mounted on high-speed maneuvering platforms," *IEEE Trans. Geosci. Remote Sens.*, vol. 57, no. 8, pp. 6018–6036, Aug. 2019.

[2] W. Li, M. Niu, Y. Zhang, Y. Huang, and J. Yang, "Forward-looking scanning radar superresolution imaging based on second-order accelerated iterative shrinkage-thresholding algorithm," *IEEE J. Sel. Topics Appl. Earth Observ. Remote Sens.*, vol. 13, pp. 620–631, 2020.

[3] S. Chen, Y. Yuan, S. Zhang, H. Zhao, and Y. Chen, "A new imaging algorithm for forward-looking missile-borne bistatic SAR," *IEEE J. Sel. Topics Appl. Earth Observ. Remote Sens.*, vol. 9, no. 4, pp. 1543–1552, Apr. 2016.

[4] Z. Li, J. Wu, Y. Huang, Z. Sun, and J. Yang, "Ground-moving target imaging and velocity estimation based on mismatched compression for bistatic forward-looking SAR," *IEEE Trans. Geosci. Remote Sens.*, vol. 54, no. 6, pp. 3277–3291, Jan. 2016.

[5] W. A. Dorigo, "Improving the robustness of cotton status characterisation by radiative transfer model inversion of multi-angular CHRIS/PROBA data," *IEEE J. Sel. Topics Appl. Earth Observ. Remote Sens.*, vol. 5, no. 1, pp. 18–29, Feb. 2012.

[6] L. Ran, Z. Liu, T. Li, R. Xie, and L. Zhang, "An adaptive fast factorized back-projection algorithm with integrated target detection technique for high-resolution and high-squint spotlight SAR imagery," *IEEE J. Sel. Topics Appl. Earth Observ. Remote Sens.*, vol. 11, no. 1, pp. 171–183, Jan. 2018.

[7] L. Ran, R. Xie, Z. Liu, L. Zhang, T. Li, and J. Wang, "Simultaneous range and cross-range variant phase error estimation and compensation for highly squinted SAR imaging," *IEEE Trans. Geosci. Remote Sens.*, vol. 56, no. 8, pp. 4448–4463, Mar. 2018.

[8] C. Cheng and G. Z. Min Xiaodong, "High-resolution forward-looking imaging algorithm for missile-borne detectors," *J. Syst. Eng. Electron.*, vol. 30, no. 3, pp. 456–466, Jun. 2019.

[9] J. Zheng et al., "An efficient strategy for accurate detection and localization of UAV swarms," *IEEE Internet Things J.*, vol. 8, no. 20, pp. 15372–15381, Oct. 2021.

[10] L. Ran, Z. Liu, L. Zhang, R. Xie, and T. Li, "Multiple local autofocus back-projection algorithm for space-variant phase-error correction in synthetic aperture radar," *IEEE Geosci. Remote Sens. Lett.*, vol. 13, no. 9, pp. 1241–1245, Sep. 2016.

[11] Y. Huang, Y. Zha, Y. Wang, and J. Yang, "Forward looking radar imaging by truncated singular value decomposition and its application for adverse weather aircraft landing," *Sensors*, vol. 15, no. 6, pp. 14397–14414, Jun. 2015.

[12] S. Kim and M.-H. Ka, "Forward-looking electromagnetic wave imaging using a radial scanning multichannel radar," *IEEE Geosci. Remote Sens. Lett.*, vol. 19, pp. 1–5, 2022.

[13] D. Mao et al., "Forward-looking geometric configuration optimization design for spaceborne-airborne multistatic synthetic aperture radar," *IEEE J. Sel. Topics Appl. Earth Observ. Remote Sens.*, vol. 14, pp. 8033–8047, 2021.

[14] Y. Zhang, Y. Zhang, Y. Huang, and J. Yang, "A sparse Bayesian approach for forward-looking superresolution radar imaging," *Sensors*, vol. 17, no. 6, p. 1353, Jun. 2017.

[15] S. Chen, C. Luo, H. Wang, B. Deng, Y. Cheng, and Z. Zhuang, "Three-dimensional terahertz coded-aperture imaging based on matched filtering and convolutional neural network," *Sensors*, vol. 18, no. 5, p. 1342, Apr. 2018.

[16] W. Huo, X. Tuo, Y. Zhang, Y. Zhang, and Y. Huang, "Balanced Tikhonov and total variation deconvolution approach for radar forward-looking super-resolution imaging," *IEEE Geosci. Remote Sens. Lett.*, vol. 19, pp. 1–5, 2021.

[17] Y. Zhang, D. Mao, Q. Zhang, Y. Zhang, Y. Huang, and J. Yang, "Airborne forward-looking radar super-resolution imaging using iterative adaptive approach," *IEEE J. Sel. Topics Appl. Earth Observ. Remote Sens.*, vol. 12, no. 7, pp. 2044–2054, Jul. 2019.

[18] Q. Zhang, Y. Zhang, Y. Huang, Y. Zhang, W. Li, and J. Yang, "Sparse with fast MM superresolution algorithm for radar forward-looking imaging," *IEEE Access*, vol. 7, pp. 105247–105257, 2019.

[19] K. Tan, W. Li, J. Pei, Y. Huang, and J. Yang, "An I/Q-channel modeling maximum likelihood super-resolution imaging method for forward-looking scanning radar," *IEEE Geosci. Remote Sens. Lett.*, vol. 15, no. 6, pp. 863–867, Jun. 2018.

[20] J. Xia, X. Lu, and W. Chen, "Multi-channel deconvolution for forward-looking phase array radar imaging," *Remote Sens.*, vol. 9, no. 7, p. 703, Jul. 2017.

[21] Y. Zhang, X. Tuo, Y. Huang, and J. Yang, "A TV forward-looking super-resolution imaging method based on TSVD strategy for scanning radar," *IEEE Trans. Geosci. Remote Sens.*, vol. 58, no. 7, pp. 4517–4528, Jul. 2020.

[22] Y. Zha, Y. Huang, Z. Sun, Y. Wang, and J. Yang, "Bayesian deconvolution for angular super-resolution in forward-looking scanning radar," *Sensors*, vol. 15, no. 3, pp. 6924–6946, Jan. 2015.

[23] J. Janjic et al., "Sparse ultrasound image reconstruction from a shape-sensing single-element forward-looking catheter," *IEEE Trans. Biomed. Eng.*, vol. 65, no. 10, pp. 2210–2218, Oct. 2018.

[24] Y. Wu, Y. Zhang, D. Mao, Y. Huang, and J. Yang, "Sparse super-resolution method based on truncated singular value decomposition strategy for radar forward-looking imaging," *J. Appl. Remote Sens.*, vol. 12, no. 3, Sep. 2018, Art. no. 035021.

[25] K. Wu, W. Cui, and X. Xu, "Superresolution radar imaging via peak search and compressed sensing," *IEEE Geosci. Remote Sens. Lett.*, vol. 19, pp. 1–5, 2022.

[26] J. Liu, S. Xu, X. Gao, and X. Li, "Novel imaging methods of stepped frequency radar based on compressed sensing," *J. Syst. Eng. Electron.*, vol. 23, no. 1, pp. 47–56, Feb. 2012.

[27] S. Tomei, A. Bacci, E. Giusti, M. Martorella, and F. Berizzi, "Compressive sensing-based inverse synthetic radar imaging imaging from incomplete data," *IET Radar, Sonar Navigat.*, vol. 10, no. 2, pp. 386–397, 2016.

[28] G. Xu, B. Zhang, H. Yu, J. Chen, M. Xing, and W. Hong, "Sparse synthetic aperture radar imaging from compressed sensing and machine learning: Theories, applications, and trends," *IEEE Geosci. Remote Sens. Mag.*, early access, Dec. 1, 2022, doi: 10.1109/MGRS.2022.3218801.

[29] C. Kreucher and M. Brennan, "A compressive sensing approach to multistatic radar change imaging," *IEEE Trans. Geosci. Remote Sens.*, vol. 52, no. 2, pp. 1107–1112, Feb. 2014.

[30] A. Bacci, D. Staglianò, E. Giusti, S. Tomei, F. Berizzi, and M. Martorella, "Compressive sensing for interferometric inverse synthetic aperture radar applications," *IET Radar, Sonar Navigat.*, vol. 10, no. 8, pp. 1446–1457, Oct. 2016.

[31] G. Xu, B. Zhang, J. Chen, F. Wu, J. Sheng, and W. Hong, "Sparse inverse synthetic aperture radar imaging using structured low-rank method," *IEEE Trans. Geosci. Remote Sens.*, vol. 60, pp. 1–12, 2021.

[32] E. Giusti, D. Cataldo, A. Bacci, S. Tomei, and M. Martorella, "ISAR image resolution enhancement: Compressive sensing versus state-of-the-art super-resolution techniques," *IEEE Trans. Aerosp. Electron. Syst.*, vol. 54, no. 4, pp. 1983–1997, Aug. 2018.

[33] S. Zhang, W. Zhang, Z. Zong, Z. Tian, and T. S. Yeo, "High-resolution bistatic ISAR imaging based on two-dimensional compressed sensing," *IEEE Trans. Antennas Propag.*, vol. 63, no. 5, pp. 2098–2111, May 2015.

[34] D. Ao, R. Wang, C. Hu, and Y. Li, "A sparse SAR imaging method based on multiple measurement vectors model," *Remote Sens.*, vol. 9, no. 3, p. 297, Mar. 2017.

[35] W. Qiu, J. Zhou, and Q. Fu, "Jointly using low-rank and sparsity priors for sparse inverse synthetic aperture radar imaging," *IEEE Trans. Image Process.*, vol. 29, pp. 100–115, 2020.

[36] X. Zhang, T. Bai, H. Meng, and J. Chen, "Compressive sensing-based ISAR imaging via the combination of the sparsity and nonlocal total variation," *IEEE Geosci. Remote Sens. Lett.*, vol. 11, no. 5, pp. 990–994, May 2014.

[37] C. Zeng, W. Zhu, X. Jia, and L. Yang, "Sparse aperture ISAR imaging method based on joint constraints of sparsity and low rank," *IEEE Trans. Geosci. Remote Sens.*, vol. 59, no. 1, pp. 168–181, Jan. 2021.

[38] L. Zhang et al., "Resolution enhancement for inversed synthetic aperture radar imaging under low SNR via improved compressive sensing," *IEEE Trans. Geosci. Remote Sens.*, vol. 48, no. 10, pp. 3824–3838, Oct. 2010.

[39] C. Lu, J. Feng, S. Yan, and Z. Lin, "A unified alternating direction method of multipliers by majorization minimization," *IEEE Trans. Pattern Anal. Mach. Intell.*, vol. 40, no. 3, pp. 527–541, Mar. 2018.

[40] H. R. Hashempour, "Sparsity-driven ISAR imaging based on two-dimensional ADMM," *IEEE Sensors J.*, vol. 20, no. 22, pp. 13349–13356, Nov. 2020.

[41] Y. Yang, S. Gui, and Q. Wan, "ISAR moving target imaging method using Hy-ADMM and mm-GLRT," *IEEE Sensors J.*, vol. 22, no. 3, pp. 2618–2629, Feb. 2022.

[42] H. R. Hashempour, "Fast ADMM-based approach for high-resolution ISAR imaging," *Electron. Lett.*, vol. 56, no. 18, pp. 954–957, Sep. 2020.

[43] D. P. Wipf and B. D. Rao, "An empirical Bayesian strategy for solving the simultaneous sparse approximation problem," *IEEE Trans. Signal Process.*, vol. 55, no. 7, pp. 3704–3716, Jul. 2007.

[44] Z. Zhang and B. D. Rao, "Sparse signal recovery with temporally correlated source vectors using sparse Bayesian learning," *IEEE J. Sel. Topics Signal Process.*, vol. 5, no. 5, pp. 912–926, Jun. 2011.

[45] S. F. Cotter, B. D. Rao, K. Engan, and K. Kreutz-Delgado, "Sparse solutions to linear inverse problems with multiple measurement vectors," *IEEE Trans. Signal Process.*, vol. 53, no. 7, pp. 2477–2488, Jul. 2005.

[46] D. Wipf and S. Nagarajan, "Iterative reweighted l_1 and l_2 methods for finding sparse solutions," *IEEE J. Sel. Topics Signal Process.*, vol. 4, no. 2, pp. 317–329, Jan. 2010.

[47] S.-H. Jung, Y.-S. Cho, R.-S. Park, J.-M. Kim, H.-K. Jung, and Y.-S. Chung, "High-resolution millimeter-wave ground-based SAR imaging via compressed sensing," *IEEE Trans. Magn.*, vol. 54, no. 3, pp. 1–4, Mar. 2018.

[48] J. Fang, S. Hu, and X. Ma, "A boosting SAR image despeckling method based on non-local weighted group low-rank representation," *Sensors*, vol. 18, no. 10, p. 3448, Oct. 2018.

[49] F. H. C. Tivive and A. Bouzerdoum, "Through the wall scene reconstruction using low rank and total variation," *IEEE Trans. Comput. Imag.*, vol. 6, pp. 221–234, 2020.